

Detecting fast-variation pulsations in solar hard X-ray and radio emissions

Dong Li,^{1,2*}

¹*Purple Mountain Observatory, Chinese Academy of Sciences, Nanjing 210023, China*

²*State Key Laboratory of Solar Activity and Space Weather, National Space Science Center, Chinese Academy of Sciences, Beijing 100190, China*

Accepted 2025 June 08. Received 2025 June 03; in original form 2025 May 01

ABSTRACT

Quasi-periodic pulsations (QPPs) at sub-second periods are frequently detected in the time series of X-rays during stellar flares. However, such rapid pulsations are rarely reported in the hard X-ray (HXR) emission of the small solar flare. We explored the QPP patterns with fast-time variations in HXR and radio emissions produced in a small solar flare on 2025 January 19. By applying the Fast Fourier Transform, the fast-variation pulsations at a quasi-period of about 1 s are identified in the HXR channel of 20–80 keV, which were simultaneously measured by the Hard X-ray Imager and the Konus-Wind. The rapid pulsations with a same quasi-period were also detected in the radio emission at a lower frequency range of about 40–100 MHz. The restructured HXR images show that the QPP patterns mainly locate in footpoint areas that connect by hot plasma loops, and they appear in the flare impulsive phase. Our observations suggest that the fast-variation pulsations could be associated with nonthermal electrons that are periodically accelerated by the intermittent magnetic reconnection, and the 1-s period may be modulated by the coalescence instability between current-carrying loops and magnetic islands.

Key words: Sun: flares – Sun: oscillations – Sun: X-rays – Sun: radio radiation

1 INTRODUCTION

The phenomenon of quasi-periodic pulsations (QPPs) is an observed feature that is a highly variable modulation to the flare emission, and it is always dominated by a series of regular, repeated and successive pulsations in the time-intensity curve of solar/stellar flares (e.g., Zimovets et al. 2021, a reference therein). The QPPs behavior is a subject of much interest, because it is important for us to understand the impulsive and periodic energy-releasing processes in the solar atmosphere, i.e., the intermittent magnetic reconnection, or the repetitive particle acceleration (e.g., Tan 2008; Yuan et al. 2019; Li et al. 2024). It was first noted by Parks & Winckler (1969) in wavebands of hard X-ray (HXR) and microwave during a solar flare. And now, such quasi-periodic behavior has been reported throughout all the electromagnetic spectrum in wavebands of radio/microwave, white light, ultraviolet (UV), extreme ultraviolet (EUV), soft and hard X-rays (SXR/HXR) (e.g., Tan et al. 2016; Nakariakov et al. 2018; Kolotkov et al. 2021; Shen et al. 2022; Motyk et al. 2023; Li, Wang, & Huang 2024; Zhou et al. 2024; Song et al. 2025). Besides, the QPPs feature has been detected in wavelengths of Ly α (Li 2022), H α (Kashapova et al. 2020), and γ -ray line at 2.223 MeV (Li & Chen 2022). Although the QPPs behavior has been observed in a large number of solar/stellar flares, the generation mechanism of flare QPPs is still an open issue (Kupriyanova et al. 2020; Zimovets et al. 2021). The flare QPPs are often associated with magnetohydrodynamic (MHD) waves (Nakariakov & Kolotkov 2020), particularly that the flare QPPs are highly related to the magnetic loop and current sheet (cf. Zimovets et al. 2021). The flare QPPs can also be triggered by the intermittent magnetic reconnection.

The idea is that nonthermal particles could be periodically accelerated by the quasi-periodic reconnection (Zhang, Li, & Ye 2024; Li et al. 2025). This model is well to produce the periodic pulsations that are observed in HXR and microwave channels during the flare impulsive phase (e.g., Clarke et al. 2021; Li et al. 2021; Kumar, Karpen, & Dahlin 2025). However, there is not a mechanism to explain all the observed QPPs, which may be attributed to the observational fact that the current data can not provide sufficient information to distinguish various models (Kupriyanova et al. 2020).

The term ‘QPPs’ generally refers to the presence of at least three successive and periodic pulsations in flare intensity curves (e.g., McLaughlin et al. 2018), although this is not a strict definition. On the other hand, the term ‘quasi-period’, which is a varying instantaneous period, is usually used for flare QPPs (Nakariakov et al. 2019). Since the first report on flare QPPs, their quasi-periods have been detected in a wide range of timescales, i.e., subseconds, several to dozens of seconds, and even hundreds of seconds (e.g., Carley et al. 2019; Knuth & Glesener 2020; Altyntsev et al. 2022; Collier et al. 2023; Zhao et al. 2023; French et al. 2024). It appears that the observed quasi-periods strongly depend upon wavebands. For instance, the quasi-periods at the order of subseconds are mostly reported in wavebands of radio or microwave (Tan et al. 2010; Karlický, Dudík, & Rybák 2024), mainly because that solar telescopes often have high temporal cadences in radio bands, i.e., with temporal cadences of a few milliseconds. On the contrary, the flare QPPs that are observed in SXR and HXR channels usually show longer quasi-periods, i.e., ≥ 4 s (Hayes et al. 2020; Collier et al. 2023). Actually, the flare QPPs at shorter quasi-periods (i.e., ≤ 1 s) have been reported in the high-energy emission of HXRs and γ -rays, and they are found to be produced in large (i.e., M- or X-class) solar flares (Knuth & Glesener 2020; Li 2025). Moreover, the sub-

* E-mail: lidong@pmo.ac.cn

second QPPs were also observed in X-rays during the stellar flare (Misra et al. 2020), suggesting that such rapid pulsations tend to appear in large flares. The newly launched Hard X-ray Imager (HXI; Su et al. 2019) on board the Advanced Space-based Solar Observatory (ASO-S) has a high temporal cadence in the burst mode, providing us with an opportunity to investigate the fast-variation pulsations in HXR emissions and localise their generated sources. In this article, we investigated a short-period QPP in HXR and radio emissions during a small flare.

2 OBSERVATIONS

We analysed a C-class solar flare that was located in the active region of NOAA 13959. It started at $\sim 16:58$ UT, peaked at $\sim 17:08$ UT, and stopped at about 17:12 UT. The solar flare was measured by the Konus-Wind (KW; Lysenko et al. 2022), ASO-S/HXI, the Spectrometer/Telescope for Imaging X-rays (STIX; Krucker et al. 2020) for the Solar Orbiter, the Geostationary Operational Environmental Satellite (GOES), the Atmospheric Imaging Assembly (AIA; Lemen et al. 2012) on board the Solar Dynamics Observatory (SDO), the Chinese H α Solar Explorer (CHASE; Li et al. 2019), the STEREO/WAVES (SWAVES), the Expanded Owens Valley Solar Array (EOVSA), and the e-CALLISTO radio spectrograph at Greenland.

KW can provide the count rate light curves in three wide energy channels with accumulation time of 2.944 s in the waiting mode, and it switches to the varying temporal cadences (e.g., 2–256 ms) in the triggered mode. ASO-S/HXI takes the imaging spectroscopy of solar flares in the high-energy range of about 10–300 keV. Its temporal cadence is normally 4 s in the regular mode and changes to be 0.25 s in the burst mode. STIX measures the solar flare in the X-ray range of 4–150 keV, and the scientific data at level 1 (i.e., L1) for this event has a temporal cadence of about 3 s. GOES can provide full-disk light curves in SXR channels of 1–8 Å and 0.5–4 Å at an uniform cadence of 1 s.

SDO/AIA takes snapshots over the entire Sun in multiple UV/EUV wavelengths. In this study, we used the synoptic images, which has a temporal cadence of 2 minutes, and a pixel scale of $2.4''$. CHASE provides the spectroscopic data of the entire Sun in the waveband of H α , and it has a pixel scale of $1.04''$, and a temporal cadence of about 71 s. SWAVES measures the solar dynamic spectrum in the frequency range of about 0.00261–16.025 MHz, and it has a temporal cadence of 1 minute. EOVSAs is a solar radioheliograph, providing the radio dynamic spectrum in frequencies of ~ 1 –18 GHz, the temporal cadence can be as high as 1 s. It can also provide microwave maps with a spatial scale of $2.5'' \text{ pixel}^{-1}$. The e-CALLISTO radio spectrograph at Greenland provides the radio dynamic spectrum in the frequency range of ~ 10 –106 MHz, which has an uniform cadence of 0.25 s.

3 METHODS AND RESULTS

Figure 1 shows an overview of the C8.2 flare in multiple wavebands. Panel (a) presents the GOES fluxes in SXR energy bands of 1–8 Å and 0.5–4 Å from 16:55 UT to 17:25 UT. The background is the radio dynamic spectrum measured by SWAVES, suggesting that a group of type III radio bursts is accompanied by the C-class solar flare. The radio bursts in the frequency range of about 20–100 MHz are also measured by the e-CALLISTO spectrograph at Greenland, and they appeared in the rise phase of the solar flare, as shown in panel (b). The overplotted curve is the radio flux at the frequency of 85.2 MHz. Figure 1 (c) presents three intensity curves in HXR energy

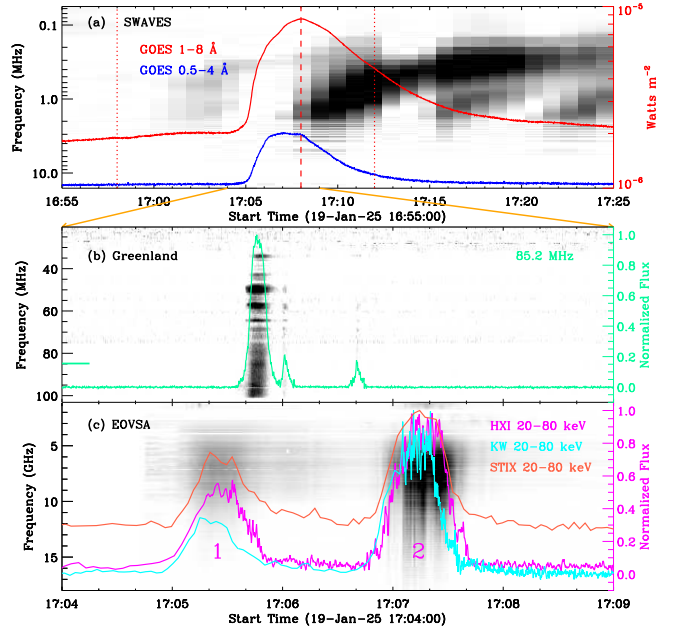


Figure 1. Overview of the C8.2 flare on 2025 January 19. (a) SXR fluxes recorded by GOES at 1–8 Å (red) and 0.5–4 Å (blue). The vertical lines marks the start, peak and stop time of the C8.2 flare. (b) Radio time series at the frequency of 85.2 MHz (spring green). (c) Normalized HXR light curves captured by HXI 20–80 keV (magenta), KW 20–80 keV (cyan) and STIX 20–80 keV (tomato). The backgrounds are radio dynamic spectra measured by SWAVES, e-Callisto, and EOVSAs respectively.

bands of HXI 20–80 keV, KW 20–80 keV, and STIX 20–80 keV during 17:04–17:09 UT. In this study, the HXI intensity curve is extracted from an open flux monitor and has a higher cadence of 0.25 s, the KW flux has been interpolated into an uniform cadence of 0.128 s, and the STIX flux is derived from the science pixelated data. The three HXR intensity curves show two main peaks, as marked by the Arabic numerals. The two main peaks can also be found in the microwave emission measured by EOVSAs. We can note that a number of repetitive and successive wiggles superimposed on the main peak 2, which might be regarded as the fast-variation pulsations, termed as ‘short-period QPP’. It is clearly observed in the intensity curves from ASO-S/HXI and KW, but not measured by STIX due to its 3-s cadence. We also note that the short-period QPP is not seen during the main peak 1, which can be attributed to the normal mode of HXI and KW.

Based on the Lomb-Scargle periodogram method (Scargle 1982), the Fast Fourier Transform (FFT) is utilized to the raw intensity curves in wavebands of HXR and radio, and their Fourier power spectra are derived. Next, a simple model (S) is applied for fitting the Fourier power spectrum, that is, a power-law distribution plus a constant (C) term (e.g., Liang et al. 2020; Anfinogentov et al. 2021), as shown in Eq. (1).

$$SP = A P^{-\alpha} C, \quad (1)$$

Where P is the period distribution of Fourier power spectra, A denotes to the amplitude of Fourier power spectra, and α represents a power-law index.

Figure 2 shows the Fourier power spectra and their best-fit results in high-energy HXR and low-frequency radio emissions. We note that two peaks are above the 99% confidence level in the HXR energy range of 20–80 keV measured by KW, corresponding to double

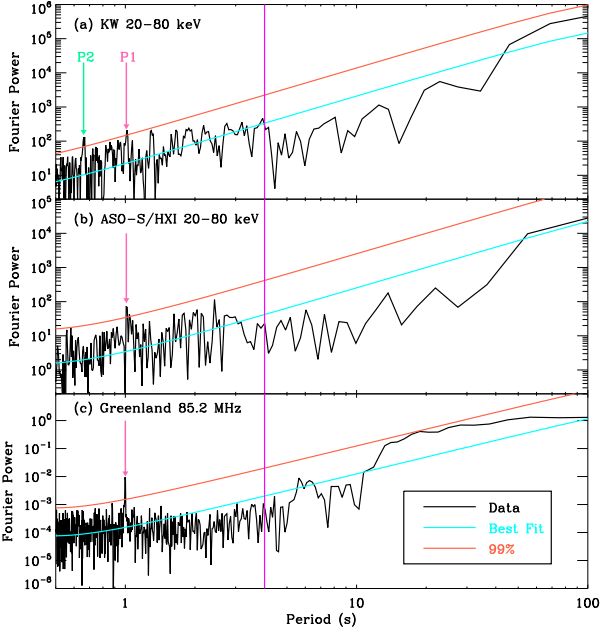


Figure 2. Fourier power spectra during the C8.2 flare in wavelengths of HXR (a & b) and radio (c). The cyan line in each panel represents the best fit for the observational data (black), the tomato line is the confidence level at 99%. The hot pink arrow outlines the interested period above the 99% confidence level.

quasi-periods at about 0.66 s and 1.0 s, as indicated by the hot pink and green arrows. On the other hand, only one peak exceeds the 99% confidence level in channels of HXI 20–80 keV and the low-frequency radio emission, confirming the existence of fast-variation pulsations with a quasi-period of about 1 s. The shorter quasi-period at about 0.66 s is not detected by ASO-S/HXI and e-CALLISTO, mainly limiting to their temporal cadence, i.e., 0.25 s. The 1-s QPP can be detected in data of three different instruments, such as two spacecrafts and one ground-based telescope, which clearly exclude instrumental artefacts and demonstrate the presence of fast-variation pulsations during the C-class flare.

In order to look closely at the fast-variation pulsations, the wavelet analysis method with a mother function of ‘Morlet’ (Torrence & Compo 1998) is used for the detrended time series in the waveband of KW 20–80 keV, since it has a higher temporal cadence of 0.128 s. The raw light curve is decomposed into a long-term trend and a detrended time series by using the Fourier method. In our case, a threshold timescale of 4 s is chosen to distinguish them, as indicated by the vertical magenta line in Figure 2.

Figure 3 presents the wavelet analysis results. Panel (a) draws the HXR flux and its long-term trend. Here, the long-term trend can be regarded as the background emission, which matches the raw light curve. Panel (b) plots the detrended time series, which has been normalized by its long-term trend. It clearly reveals the QPP patterns at a shorter period when the KW instrument switches to the triggered mode. The modulation depth, which can be determined by the ratio between the detrended time series and its long-term trend, is more than 10% during these fast-variation pulsations. It can be as high as 20% in some rapid pulsations, while it is rather small (i.e., <3%) after the QPP patterns. Panels (c) & (d) show the wavelet power spectrum and its Global wavelet power spectrum. They are both characterized by a bulk of power spectrum inside the 99% confidence level, which are centered at about 1 s. Also, these two

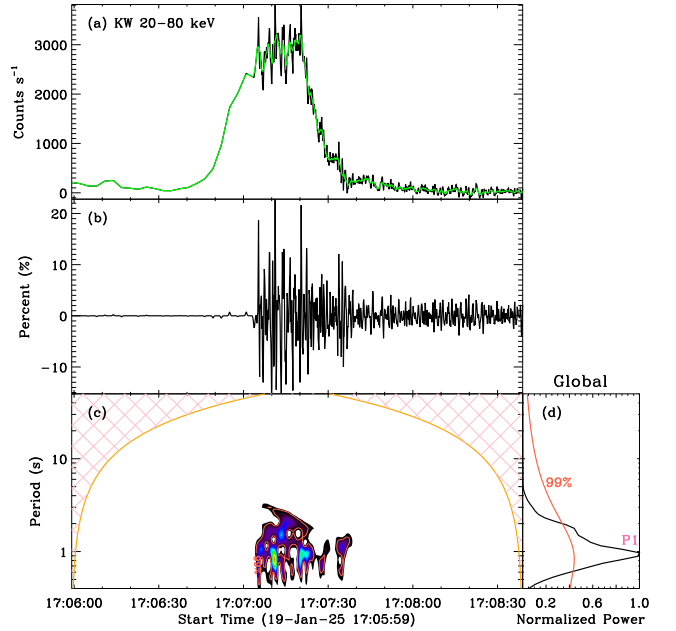


Figure 3. Morlet wavelet analysis for the HXR flux of the C8.2 flare. (a) Raw light curve at KW 20–80 keV. The overlaid green lines represent its long-term trend. (b) Detrended time series normalized to the maximum of the long-term trend. (c) Morlet wavelet power spectrum for the detrended time series. (d) Global wavelet power spectrum. The tomato contours or lines indicate a significance level of 99%.

power spectra show a wide period range, which may be attributed to the lower resolution of the wavelet analysis method, and this matches two quasi-periods obtained from the FFT method in Figure 2 (a). The 1-s QPP patterns appear during the flare impulsive phase, i.e., roughly from 17:07:05 UT to 17:07:35 UT. All these observations demonstrate that the short-period QPP comes from the solar flare rather than the solar background emission.

Figure 4 shows the spatial structure of the C8.2 flare in multiple wavelengths of HXR, microwave, H α , and UV/EUV. Panel (a) draws a HXR map in the high-energy range of 20–80 keV, the overplotted contours represent the HXR (cyan) and microwave (magenta) radiation. In this case, the HXR map is reconstructed from the ASO-S/HXI data with an algorithm of HXI_CLEAN, and it exhibits several HXR radiation sources, which match those UV bright kernels in the photosphere seen in the wavelength of AIA 1700 Å, as shown in panel (b). These HXR sources or UV kernels may be regarded as the conjugate points that connected by hot plasma loops, and the loop-top source can be seen in passbands of microwave or HXR, as indicated by the magenta contour. Panel (c) & (d) shows the EUV maps in wavebands of AIA 304 Å and 131 Å, which contain the lower (~ 0.05 MK) and higher (~ 10 MK) temperature plasmas, respectively. Some ribbon-like structures are observed in wavebands of AIA 304 Å and CHASE H α 6562.82 Å, and they are overlapping on the UV kernels or HXR sources, indicating that those ribbon-like structures are flare ribbons. Two loop-like features can be clearly seen in the AIA 131 Å map, and they connect those flare ribbons or kernels through the loop-top region, as outlined by the blue, green, and magenta contours. These observations suggest that the main HXR sources could be regarded as footpoints, and the strongest microwave emission may locate at the loop-top source. The HXR sources at footpoints may contain a series of magnetic islands that are formed in opposite magnetic polarities. Assuming a semi-circular profile of

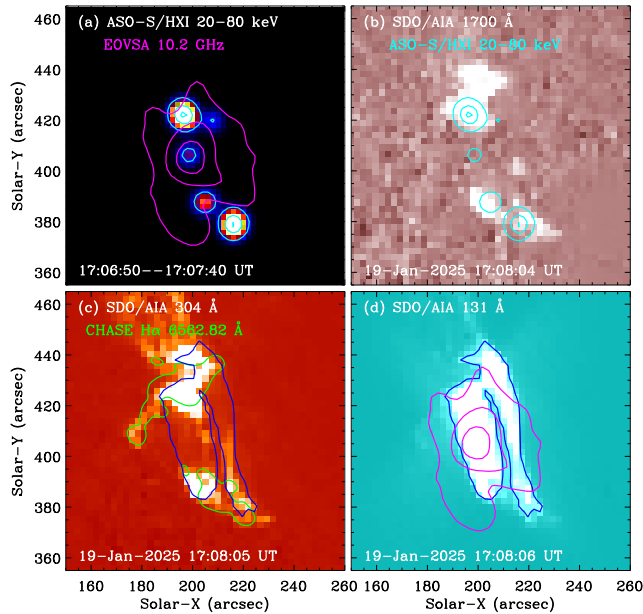


Figure 4. Multi-wavelength images with a FOV of $\sim 110'' \times 110''$ during the C8.2 flare. (a) HXR map in the energy range of HXI 20–80 keV. The contours represent the HXR (cyan) and microwave (magenta) emissions, respectively, and their contour levels set at 10%, 50%, and 90% in the HXR channel, while those are 20%, 50%, and 80% in the microwave emission. (b) UV map at AIA 1700 Å. (c & d) EUV maps in wavelengths of AIA 304 and 131 Å. The color contours outline flare ribbons at $H\alpha$ 6562.82 Å (green) and hot loops at AIA 131 Å (blue), respectively.

flare loops (cf. [Li & Chen 2022](#)), the loop length (L) may be estimated by the distance between the flare ribbons or kernels, which is in the range of 40–65 Mm.

4 CONCLUSION AND DISCUSSION

We present an observational detection of 1-s QPP of HXR and radio emissions produced in a small solar flare on 2025 January 19. The fast-variation pulsations in channels of HXR and low-frequency radio are detected by ASO-S/HXI, KW, and e-CALLISTO, mainly benefiting from the high-cadence burst mode of the three telescopes. Combining the Fourier Transform ([Anfinogentov et al. 2021](#)) and wavelet analysis ([Torrence & Compo 1998](#)) method, the quasi-period centered at about 1 s is simultaneously identified in passbands of KW 20–80 keV, HXI 20–80 keV, and Greenland 85.2 MHz. The presence of fast-variation pulsations in data of three different instruments on two spacecrafts and one ground-based telescope clearly excludes the instrumental artefact. The modulation depth of the 1-s QPP is in the range of about 10%–20%, which is close to that of flare QPPs at longer periods in HXRs and γ -rays ([Li & Chen 2022](#)).

Generally, the very-short period pulsations (i.e., $\ll 1$ s) were often reported in solar radio emissions, especially in the microwave regime (e.g., [Tan et al. 2010](#); [Nakariakov et al. 2018](#); [Karlický, Dudík, & Rybák 2024](#)). Conversely, the flare QPPs in high-energy emissions are usually found to show the characteristic periods above 4 s (e.g., [Parks & Winckler 1969](#); [Li & Chen 2022](#); [Collier et al. 2023](#); [Inglis & Hayes 2024](#)), which may be attributed to the observational limitation, for instance, the signal-to-noise ratio of solar telescopes in channels of HXRs or γ -rays is a bit low. By statis-

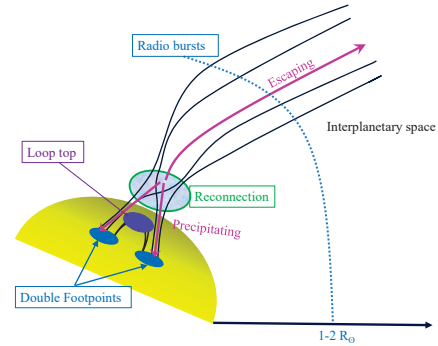


Figure 5. Cartoon of the flare and the type III radio bursts, which is used for illustrating the likely mechanism that was observed the particle acceleration resulting in QPPs in radio/microwave and HXR emissions. The QPP source regions such as the loop top and double footpoints are related to the open and closed field lines that allows for the escaping (or upward) and precipitating (or downward) electrons.

tically investigating the solar flares measured by Fermi/GBM in the high-cadence burst mode, [Inglis & Hayes \(2024\)](#) demonstrate that the short-period QPPs at the timescale of about 1–4 s are actually existing in the HXR channel, but they are not widespread. Recently, the fast-variation pulsations at quasi-periods that is not more than 1 s have been detected in the high-energy range of HXR and γ -ray continuum during large solar flares, i.e., a M-class ([Knuth & Glesener 2020](#)) and an X-class flares ([Li 2025](#)). In our case, the fast-variation pulsations at a quasi-period of about 1 s is simultaneously observed in passbands of HXR and low-frequency radio emissions during a small flare. Moreover, the spatial structure of the QPP patterns is reconstructed using the ASO-S/HXI data, providing us an opportunity to explore their generation mechanism.

The QPP patterns are frequently interpreted as MHD waves (e.g., [Nakariakov & Kolotkov 2020](#)). Here, the phase speed (v_p) may be determined by the flare loop length (L) and the quasi-period (P), which is $v_p = 2LP \approx 0.8 - 1.3 \times 10^5 \text{ km s}^{-1}$. The phase speed is approximately equal to $(0.27-0.43)c$ ($c \approx 3 \times 10^5 \text{ km s}^{-1}$ is the speed of light), and it is much faster than the local sound and Alfvén speeds. Thus, the short-period QPP is difficult to be modulated by the MHD wave. We also note that the 1-s QPP tends to appear in the impulsive phase of the C8.2 flare, and it can be simultaneously seen in HXR and low-frequency radio emissions, implying the existence of nonthermal electrons. Therefore, the flare QPP might be triggered by a periodic regime of magnetic reconnection, which may periodically accelerate nonthermal electrons, as shown in Figure 5. Briefly, the pulsed nonthermal electrons are accelerated by the magnetic reconnection and show bi-directional propagations, as indicated by the magenta arrows. The downward electron precipitates toward the lower atmosphere along the closed magnetic field line, leading to the HXR or microwave pulsation at double footpoints or loop-top regions. On the other hand, the upward electron escapes along the open magnetic field line and produces the low-frequency radio pulsation in the interplanetary space, i.e., type III radio bursts. Such reconnection process occurs repeatedly and regularly, generating the fast-variation pulsations at a quasi-period in HXR and low-frequency radio emissions ([Clarke et al. 2021](#); [Li et al. 2021](#)). The short quasi-period at about 1 s might be explained by the current-loop coalescence model presented by [Tajima et al. \(1987\)](#), who have demonstrated that the timescale of transit pulsations in the range of 1–10 s could be modulated by the coalescence instability of current-carrying loops and magnetic is-

lands. In this model, the magnetic islands are located in current sheets that are generated by the interaction of various magnetic loops with opposite magnetic polarities. The coalescence instabilities between magnetic loops and current sheets with a quasi-period would cause periodic energy releases in the solar flare (e.g., [Zhao et al. 2023](#)), that is, a periodic regime of magnetic reconnection occurs during the flare impulsive phase. The detection of HXR sources indicates some magnetic islands, and the observation of hot plasma loops rooted in different footpoints suggests various magnetic loops with opposite magnetic polarities, although the current sheets are not seen in our case due to the observational limitation, i.e., the lower spatial resolution. It has been demonstrated that the current-carrying loop itself is easily exciting a tearing-mode oscillation, modulating the magnetic reconnection process and generating a QPP pattern at quasi-periods ranging from sub-seconds to a few seconds (cf. [Tan 2010](#); [Tan & Tan 2012](#)). Therefore, we may conclude that the fast-variation pulsations at a quasi-period of 1 s is probable associated with the intermittent magnetic reconnection due to the coalescence of current-carrying loops.

ACKNOWLEDGEMENTS

This work is funded by the National Key R&D Program of China 2022YFF0503002 (2022YFF0503000) and 2021YFA1600502 (2021YFA1600500), the Strategic Priority Research Program of the Chinese Academy of Sciences, Grant No. XDB0560000. D. Li is also supported by the Specialized Research Fund for State Key Laboratory of Solar Activity and Space Weather. We thank the teams of ASO-S/HXI, KW, STIX, GOES, SDO, CHASE, and e-CALLISTO for their open data use policy.

DATA AVAILABILITY

Publicly available data was analyzed and they can be found here: <http://aso-s.pmo.ac.cn/sodc/dataArchive.jsp>, <https://www.ioffe.ru/LEA/kwsun/>, <http://jsoc.stanford.edu/>, <https://datacenter.stix.i4ds.net/stix>, <https://soleil.i4ds.ch/sollarradio/callistoQuicklooks/>.

REFERENCES

Anfinogentov S. A., Nakariakov V. M., Pascoe D. J., Goddard C. R., 2021, *ApJS*, 252, 11.
 Altynsev A. T., Meshalkina N. S., Sych R. A., Kolotkov D. Y., 2022, *A&A*, 663, A149.
 Carley E. P., Hayes L. A., Murray S. A., Morosan D. E., Shelley W., Vilmer N., Gallagher P. T., 2019, *NatCo*, 10, 2276.
 Clarke B. P., Hayes L. A., Gallagher P. T., Maloney S. A., Carley E. P., 2021, *ApJ*, 910, 123.
 Collier H., Hayes L. A., Battaglia A. F., Harra L. K., Krucker S., 2023, *A&A*, 671, A79.
 French R. J., Hayes L. A., Kazachenko M. D., Reeves K. K., Shen C., Lörinčík J., 2024, *ApJ*, 977, 207.
 Hayes L. A., Inglis A. R., Christe S., Dennis B., Gallagher P. T., 2020, *ApJ*, 895, 50.
 Inglis A. R., Hayes L. A., 2024, *ApJ*, 971, 29.
 Kashapova L. K., Kupriyanova E. G., Xu Z., Reid H. A. S., Kolotkov D. Y., 2020, *A&A*, 642, A195.
 Karlický M., Dudík J., Rybák J., 2024, *SoPh*, 299, 113.
 Kolotkov D. Y., Nakariakov V. M., Holt R., Kuznetsov A. A., 2021, *ApJL*, 923, L33.

Kumar P., Karpen J. T., Dahlin J. T., 2025, *ApJ*, 980, 158.
 Knuth T., Glesener L., 2020, *ApJ*, 903, 63.
 Krucker S., Hurford G. J., Grimm O., Kögl S., Gröbelbauer H.-P., Etesi L., Casadei D., et al., 2020, *A&A*, 642, A15.
 Kupriyanova E., Kolotkov D., Nakariakov V., Kaufman A., 2020, *STP*, 6, 3.
 Lemen J. R., Title A. M., Akin D. J., Boerner P. F., Chou C., Drake J. F., Duncan D. W., et al., 2012, *SoPh*, 275, 17.
 Li C., Fang C., Li Z., Ding M.-D., Chen P.-F., Chen Z., Lin L.-K., et al., 2019, *RAA*, 19, 165.
 Li D., Ge M., Dominique M., Zhao H., Li G., Li X., Zhang S., et al., 2021, *ApJ*, 921, 179.
 Li D., Chen W., 2022, *ApJL*, 931, L28.
 Li D., 2022, *ScChE*, 65, 139.
 Li D., Li J., Shen J., Song Q., Ji H., Ning Z., 2024, *A&A*, 690, A39.
 Li D., Wang J., Huang Y., 2024, *ApJL*, 972, L2.
 Li D., 2025, *A&A*, 695, L4.
 Li D., Yuan D., Yan J., Zhao X., Wu Z., Wang J., Hou Z., et al., 2025, *JGRA*, 130, e2025JA033772.
 Liang B., Meng Y., Feng S., Yang Y., 2020, *Ap&SS*, 365, 40.
 Lysenko A. L., Ulanov M. V., Kuznetsov A. A., Fleishman G. D., Frederiks D. D., Kashapova L. K., Sokolova Z. Y., et al., 2022, *ApJS*, 262, 32.
 McLaughlin J. A., Nakariakov V. M., Dominique M., Jelínek P., Takasao S., 2018, *SSRv*, 214, 45.
 Misra R., Rawat D., Yadav J. S., Jain P., 2020, *ApJL*, 889, L36.
 Motyk I. D., Kashapova L. K., Setov A. G., Shamsutdinova Y. N., Kupriyanova E. G., 2023, *Ge&Ae*, 63, 1062.
 Nakariakov V. M., Anfinogentov S., Storozhenko A. A., Kurochkin E. A., Bogod V. M., Sharykin I. N., Kaltman T. I., 2018, *ApJ*, 859, 154.
 Nakariakov V. M., Kolotkov D. Y., Kupriyanova E. G., Mehta T., Pugh C. E., Lee D.-H., Broomhall A.-M., 2019, *PPCF*, 61, 014024.
 Nakariakov V. M., Kolotkov D. Y., 2020, *ARA&A*, 58, 441.
 Parks G. K., Winckler J. R., 1969, *ApJL*, 155, L117.
 Scargle J. D., 1982, *ApJ*, 263, 835.
 Shen Y., Yao S., Tang Z., Zhou X., Qu Z., Duan Y., Zhou C., et al., 2022, *A&A*, 665, A51.
 Song D.-C., Dominique M., Zimovets I., Li Q., Li Y., Yu F., Su Y., et al., 2025, *ApJL*, 983, L41.
 Su Y., Liu W., Li Y.-P., Zhang Z., Hurford G. J., Chen W., Huang Y., et al., 2019, *RAA*, 19, 163.
 Tan B., 2008, *SoPh*, 253, 117.
 Tan B., Zhang Y., Tan C., Liu Y., 2010, *ApJ*, 723, 25.
 Tan B., 2010, *Ap&SS*, 325, 251.
 Tan B., Tan C., 2012, *ApJ*, 749, 28.
 Tan B., Yu Z., Huang J., Tan C., Zhang Y., 2016, *ApJ*, 833, 206.
 Tajima T., Sakai J., Nakajima H., Kosugi T., Brunel F., Kundu M. R., 1987, *ApJ*, 321, 1031.
 Torrence C., Compo G. P., 1998, *BAMS*, 79, 61.
 Yuan D., Feng S., Li D., Ning Z., Tan B., 2019, *ApJL*, 886, L25.
 Zhang Y., Li T., Ye J., 2024, *ApJ*, 972, 122.
 Zhao H.-S., Li D., Xiong S.-L., Zhang Y.-Q., Su Y., Chen W., Zhao Y., et al., 2023, *SCPMA*, 66, 259611.
 Zhou X., Shen Y., Yuan D., Keppens R., Zhao X., Fu L., Tang Z., et al., 2024, *NatCo*, 15, 3281.
 Zimovets I. V., McLaughlin J. A., Srivastava A. K., Kolotkov D. Y., Kuznetsov A. A., Kupriyanova E. G., Cho I.-H., et al., 2021, *SSRv*, 217, 66.

This paper has been typeset from a $\text{\TeX}/\text{\LaTeX}$ file prepared by the author.